Geomech. Geophys. Geo-energ. Geo-resour. (2023) 9:31
https://doi.org/10.1007/s40948-023-00564-w

RESEARCH

Hydrostatic, strike-slip and normal stress true triaxial hydrofracturing testing of Blanco Mera Granite: breakdown pressure and tensile strength assessment

Andrea Muñoz-Ibáñez · Miguel Herbón-Penabad · Jordi Delgado-Martín · Leandro Alejano-Monge · José Alvarellos-Iglesias · Jacobo Canal-Vila

Received: 5 October 2022 / Accepted: 8 February 2023

Abstract We have designed and built a versatile testing device to perform hydraulic fracturing experiments under true triaxial conditions. The device, based on a stiff biaxial frame that can be installed in a servocontrolled press, can accommodate cube rock samples of up to 150 mm-edge. Using a low-permeability rock known as Blanco Mera granite, we have performed a series of tests across a range of confining pressures including hydrostatic, normal, and strike-slip regimes. We have verified the applicability of two simple fracture mechanics-based models for the interpretation of experimental results, and we have determined the value of tensile strength of the rock from the injection curves recorded. The orientation of the hydraulically-triggered fractures with respect to the applied stress has also been analyzed. Although the models proposed by Rummel and Abou-Sayed provided reasonably satisfactory results, especially for hydrostatic and strike-slip tests, the presence of heterogeneities and defects in the rock matrix may have a strong influence on the fracture behavior and, therefore, affect the interpretation of hydrofracturing tests.

Article Highlights

- We assess the performance of an experimental device designed to perform hydraulic fracturing tests under true triaxial loading.
- Breakdown pressure results can be reasonably estimated using fracture mechanics approaches.
- The values of tensile strength computed from the injection curves recorded under a range of confining pressures were consistent.

Keywords Hydraulic fracturing · Breakdown pressure · Tensile strength · Fracture orientation

A. Muñoz-Ibáñez · M. Herbón-Penabad · J. Delgado-Martín (✉)
Department of Civil Engineering, University of A Coruña, Campus de Elviña s/n, 15071 A Coruña, Spain
e-mail: jorge.delgado@udc.es

A. Muñoz-Ibáñez
e-mail: andrea.munozibanez@kaust.edu.sa

A. Muñoz-Ibáñez · L. Alejano-Monge
GESSMin Group, Department of Natural Resources and Environmental Engineering, CINTECX, University of Vigo, As Lagoas-Marcosende, 36310 Vigo, Spain

Present Address:
A. Muñoz-Ibáñez
Physical Science and Engineering Division, King Abdullah University of Science and Technology, Thuwal 23955-6900, Saudi Arabia

J. Alvarellos-Iglesias · J. Canal-Vila
Repsol Tecnology Laboratory, C/ Agustín de Betancourt s/n, 28935 Móstoles, Spain

Published online: 16 March 2023

1 Introduction

The exploitation of subsurface energy resources such as unconventional oil and gas or geothermal energy depends on the successful development of fracture networks (Gehne et al. 2020). In this regard, hydraulic fracturing has been widely used as a stimulation technique to promote fracture initiation and propagation in deep reservoirs. The process of hydraulic fracturing consists in the high-pressure injection of fluid into a rock mass through a borehole, where pressurization is accomplished by isolating a given section with packers (Ødegaard and Nilsen 2021). Although fluid is usually delivered with a continuous flow rate, other injection schemes (e.g., sinusoidal law or pulsating hydraulic fracturing; Zhu and Dong 2022) have been used. The hydraulic fracturing process not only generates new conductive fluid paths but also improves the connectivity of pre-existing fractures (Lu et al. 2013; Zhang et al. 2022b). Therefore, this technology can be successfully used to enhance recovery of valuable resources in low-permeability brittle media (Zhang et al. 2018; Bi et al. 2021).

Hydraulic fracturing is governed by a number of physical and mechanical parameters, such as in-situ stress, fluid pressure as well as intrinsic rock properties (porosity, permeability, tensile strength, fracture toughness, etc.; Gehne et al. 2020; Zhang et al. 2021a). Consequently, for the successful implementation of a hydrofracturing design, it is crucial to understand in detail the conditions governing fracture initiation and propagation. Worth mentioning among them are the so-called breakdown (P_B), fracture propagation (P_{prop}), or closure (P_C) pressures.

Rock masses in the subsurface are in a state of true triaxial stress (Liu et al. 2018). The three orthogonal principal stresses in which the anisotropic stress conditions can be resolved are generated through multiple sources, including tectonics, overburden, sedimentation, and other geological processes (Frash et al. 2014). Accordingly, three types of stress regimes can be defined depending on the relative magnitude of the vertical and horizontal stresses. Under normal stress regime conditions, usually found in tectonically passive or extensional environments, the vertical stress (σ_V) produced by the weight of the overburden material and pore fluid is maximum. Contrary, under reverse faulting stress regime, which occurs at shallow depths or in tectonically compressed areas, σ_V is the minimum principal stress. In a strike-slip environment, the vertical stress is larger than the minimum horizontal stress (σ_h) but lower than the maximum horizontal stress (σ_H). Since fractures propagate along the path of least resistance, the direction and geometry of hydraulic fractures is highly dependent on the in-situ stress state: while in normal and strike-slip regimes the fractures should grow vertically (i.e., perpendicularly to the minimum horizontal stress), in reverse faulting stress regimes hydraulic fractures are expected to propagate horizontally (Zhang 2019). Therefore, for successful design and performance of hydraulic fracturing projects, it is necessary to understand the fracture evolution processes of the rock under true triaxial conditions (Zeng et al. 2018; Cao et al. 2021).

At laboratory-scale, mini-frac tests are useful to estimate reservoir parameters at similar stress conditions to those encountered in the field. Early laboratory hydrofracturing experiments were mainly focused on the behaviour of conventional pseudo-triaxial tests performed on hollow cylindrical samples. Because of the intrinsic experimental concept of pseudo-triaxial testing (where only maximum and minimum principal stresses are considered and the effect of a differential horizontal stress is neglected), these tests cannot completely reproduce the behaviour of rocks under in-situ conditions (Patel et al. 2018). However, to overcome this issue, a growing number of studies are addressing the importance of applying true triaxial stress conditions (i.e., main stresses are independently applied in three orthogonal directions) over parallelepiped rock samples (Huang and Liu 2017; Lu et al. 2020; Zhuang et al. 2020a).

In this contribution, we report a series of hydrofracturing experiments performed under true triaxial conditions (hydrostatic, normal, and strike-slip stress regimes) using 150 mm-edge cubic Blanco Mera granite samples. The experiments have been carried out in a specially-designed stiff biaxial frame installed in a servo-hydraulically controlled press. The analysis of the experimental results obtained is focused on the following aspects: 1) the assessment of the consistency in the orientations of the hydraulically-triggered fractures with respect to the applied stress field; and 2) the interpretation of the fluid injection curves, including the assessment of parameters such as the breakdown pressure or the tensile strength of the tested rock.

2 State of the art

2.1 Breakdown pressure (PB)

In hydraulic fracturing, breakdown pressure (P_B) corresponds to the peak pressure recorded in the injection curve (Fig. 1). It can be seen as the threshold pressure that separates stable and unstable fracture propagation (Feng et al. 2015). Although the fracture initiation pressure (i.e., the starting of the non-linear elastic phase; P_i) might be lower than P_B, it is usually more difficult to identify in the injection curves (Bröker and Ma 2022). Therefore, breakdown pressure can be taken as the upper limit of P_i. In the literature there are two conventional expressions for assessing P_B in terms of the far-field stresses. In the particular case of a vertical borehole, Hubbert and Willis (1957) derived an expression useful to compute P_B assuming that the rock is an impervious (i.e., the fluid does not penetrate the rock matrix around the borehole) linear-elastic material:

$$P_B = 3\sigma_h - \sigma_H + \sigma_T - P_0 \tag{1}$$

where σ_h and σ_H are the minimum and maximum horizontal stresses, respectively, σ_T is the tensile strength of the material, and P_0 is the pore pressure. For pervious formations with fluid penetration, Haimson and Fairhurst (1969) derived an alternative expression considering the poroelastic behaviour of the material near the borehole:

$$P_B = \frac{3\sigma_3 - \sigma_2 + \sigma_T - 2\left[\frac{\alpha(1-2\nu)}{2(1-\nu)}\right]P_0}{2\left(1 - \left[\frac{\alpha(1-2\nu)}{2(1-\nu)}\right]\right)} \tag{2}$$

where ν is the Poisson's ratio and α is the Biot's poroelastic coefficient (Biot 1941), which depends on rock porosity and its geometry. Although in these two classical approaches the borehole region is assumed to be elastic, homogenous, and defect-free, the specific geological circumstances in a given material determine the existence of pre-existent cracks. To overcome this limitation and to tackle the role of defects in the practical interpretation of the hydrofracturing experiments, other complementary approaches based on fracture mechanics have been developed. Fracture mechanics states that, in mode I (i.e., tensile opening mode), a newly formed or pre-existing crack will start to propagate when the stress intensity factor at the crack tip (K_I) reaches the corresponding mode I fracture toughness of the rock (K_{IC}). Based on that, Abou-Sayed et al. (1978) proposed the following expression applied to an infinite plate with two symmetrical fractures perpendicular to the axis of a borehole:

$$P_B = [1 - I(\beta)]\sigma_h + I(\beta)\sigma_H + \frac{K_{IC}}{f\sqrt{\pi a}} \tag{3}$$

where a is the length of the pre-existing fracture, R is the radius of the borehole, and f and g are functions of the a/R ratio. The function $I(\beta)$ depends on β, which is the inclination angle of the crack:

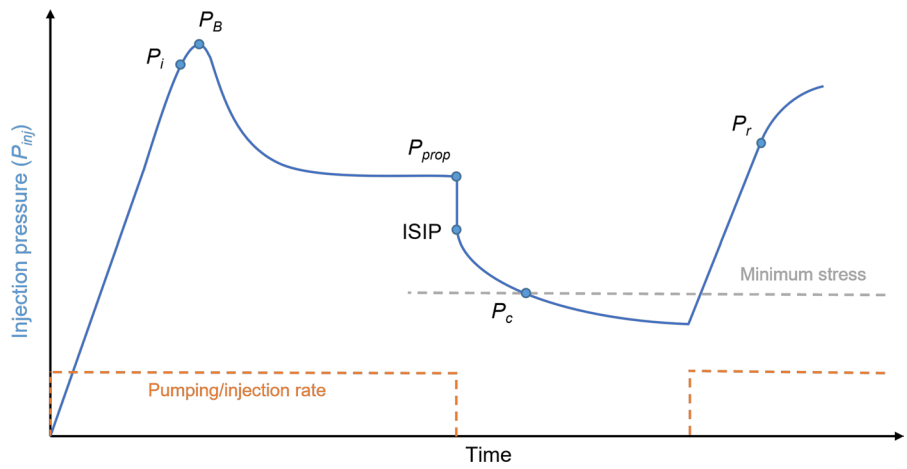

Fig. 1 Evolution of an injection curve in a hydrofracturing test. P_i (fracture initiation pressure), P_B (breakdown pressure), P_{prop} (propagation pressure), ISIP (instantaneous shut-in pressure), P_C (closure pressure) and P_r (reopening pressure)

$$I(\beta) = cos^2\beta - \frac{g}{f}cos2\beta \tag{4}$$

For fractures that are perpendicular to σ_h, the function $I(\beta)$ becomes zero, and the computation of P_B reduces to:

$$P_B = \sigma_h + \frac{K_{IC}}{f\sqrt{\pi a}} \tag{5}$$

On the other hand, Rummel (1987) assessed the value of the breakdown pressure assuming the presence of a symmetrical double-crack, oriented parallel to the direction of σ_h, in a plate containing a borehole:

$$P_B = \frac{1}{\left(h_0(b) + h_a(b)\right)}\left(\frac{K_{IC}}{\sqrt{R}} + f(b)\sigma_H + g(b)\sigma_h\right) \tag{6}$$

where b is the normalized fracture length ($b = 1 + a/R$). The functions h_0, h_a, f and g were equated by this author as follows:

$$h_0(b) = 1.3\frac{b-1}{1+b^{1.5}} + 7.8\frac{sin\left[(b-1)/2\right]}{2b^{2.5} - 1.7} \tag{7}$$

$$h_a(b) = \lambda(\pi b)^{0.5}\left(1 - \frac{2}{\pi}sin^{-1}\frac{1}{b}\right) \tag{8}$$

$$f(b) = -2\left[\left(b^2-1\right)/\pi b^7\right]^{0.5} \tag{9}$$

$$g(b) = (\pi b)^{0.5}\left(1 - \frac{2}{\pi}sin^{-1}\frac{1}{b}\right) + 2\left(b^2-1\right)\left[\frac{\left(b^2-1\right)}{\pi b^7}\right]^{0.5} \tag{10}$$

In Eq. (8) λ represents a coefficient related with the internal fracture pressure and it varies between 0 and 1.

2.2 Pressure evolution after breakdown pressure

Figure 1 shows the idealized injection curve of a typical hydraulic fracturing test. Once P_B is reached, the injection pressure drops because the volume expansion induced by fracture generation and fast propagation may be greater than the rate of fluid injection (Zhang et al. 2021a). If fluid injection continues, a relatively steady pressure may be reached and this value, which is known as fracture propagation pressure (FPP or P_{prop}), corresponds to the pressure at which unstable fracture growth proceeds. In order to keep a steady injection pressure value, injection and propagation rates must be proportional. If, at some time, fluid pumping is arrested, the pressure gradient along the fracture will reduce and fluid pressure would drop very fast to the so-called instantaneous shut-in pressure (ISIP or P_{ISIP}). This value is slightly lower than FPP. Assuming that the fracture propagates in the direction perpendicular to the minimum stress, the pressure required to hold the fracture open would be equal to σ_h. Therefore, as the fracture closes, pressure drops until reaching a value known as fracture closure pressure (FCP or P_C), which is the minimum pressure required to maintain the fracture open. P_C can be assumed to be equal to the minimum horizontal stress as far as the fracture propagates well beyond (at least four drillhole radii) the area of stress perturbation created by the presence of the drillhole (Malik et al. 2016; Bérard et al. 2019).

2.3 Tensile strength

If flow rate is kept constant during a second re-injection cycle, the peak pressure obtained is referred to as fracture re-opening pressure (FRP or P_r). Considering that the fracture was created during the first injection cycle, the difference between breakdown and re-opening pressures will correspond to the intact tensile strength (σ_T) of the tested rock (Haimson 1980):

$$\sigma_T = P_B - P_r \tag{11}$$

Although, in general, P_r can be identified as a second maximum in the injection curve, sometimes this feature may not be well-defined. To cope with this situation, some authors have assumed that FRP corresponds to the point of the curve where the injection pressure loses linearity or, said in other words, the starting point of the non-linear (inelastic) phase (Morawietz et al. 2020; Bröker and Ma 2022). In this regard, Song et al. (2001) have reported that the initial slope of the injection and re-injection curves may be very similar, provided that the flow rate is kept constant (Haimson 1980) and that the fracture closes completely between cycles (Lee and Haimson 1989). Consequently, the point where the slope of the subsequent pressurization cycles deviates from that of the first one could be taken as equal to P_r.

Finally, if the hydraulic fracturing test is performed in the absence of confining pressure ($\sigma_V = \sigma_H = \sigma_h = 0$), then P_B would correspond to the tensile strength of the material (Guo et al. 1993; Zhuang et al. 2020b). This implies to assume that the rock is almost impervious and that the influence of pore pressure over tensile strength may be neglected (Molenda et al. 2013).

2.4 Fracture orientation

It is expected that, under a non-hydrostatic regime, the fractures initiated due to fluid injection would propagate perpendicular to σ_h, which is the direction of the minimum resistance. However, even under hydrostatic conditions, the mere presence of the borehole in the rock sample induces a local region where far field stresses are disturbed and where new fractures are likely expected to grow due to the high-stress concentration.

3 Materials and methods

3.1 Materials and specimen preparation

The hydrofracturing tests were conducted using Blanco Mera granite samples. This is a bright-white, coarse-grained (1–6 mm), low porosity (1.2–1.3%) igneous rock of moderate strength (uniaxial compressive strength $\sigma_c = 100$–130 MPa; indirect tensile strength $\sigma_T = 7.5$–11 MPa) when compared with other similar rocks reported in the literature. The static Young's modulus (E) and Poisson's ratio (v) of the Blanco Mera granite are 53 GPa and 0.28–0.30, respectively (Alejano et al. 2021).

We used cubic blocks (150 mm-edge) that were drilled with a vertical drill press and a water/oil-cooled 6 mm-OD diamond drill bit perpendicular to one of their faces (Fig. 2a). For each sample, the drillhole was located in the geometric center of the face and perforated to a depth of ~ 75 mm-length (i.e., to the geometric center of the cube). After drilling, the drillhole was flushed with water to clean up the debris. Then, the sample was oven-dried at 100 °C for 24 h to remove the moisture content from the material. Upon cooling to room temperature, a high-pressure 1/8''-OD (3.175 mm) stainless steel pipe threaded in one end was inserted into the drillhole up to a depth of ~ 50 mm, leaving a cavity of ~ 25 mm-length for fluid pressurization (Fig. 2b). Care was paid to ensure that the pipe remained vertically aligned and centered with respect to the drillhole axis. The pipe was glued to the drillhole wall using a low-viscosity, two-component epoxy cement (*Fantasy Resin, Fantasy Craft*) (Fig. 2c). To prevent the penetration of the cement into the open end of the pipe, and to create a cavity for oil injection, we used a micro-packer system consisting of a coaxial flexible polymeric sleeve that is then compressed between two M3-nuts located at the edge of the previously threaded pipe. The epoxied sample was oven-dried at 60 °C for 3 h and, prior to testing, the tube was bent 90° (to make possible the

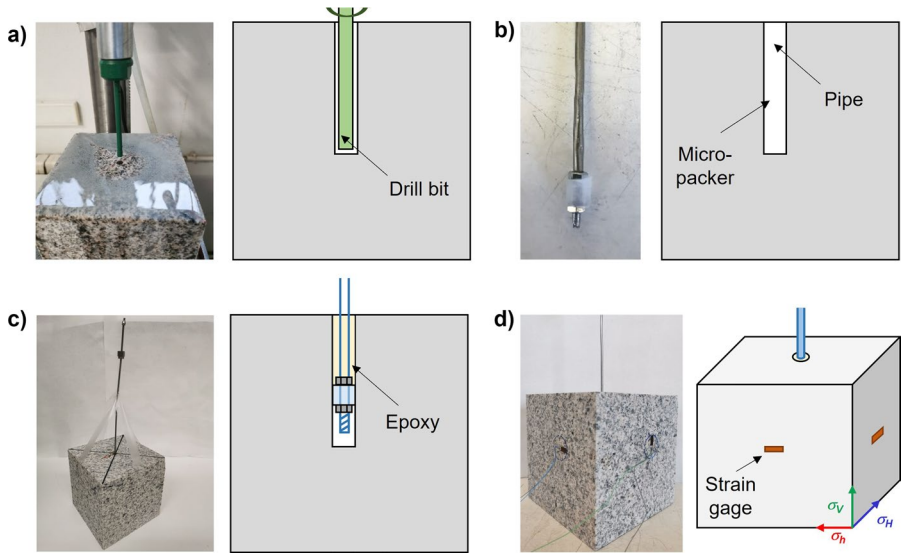

Fig. 2 Sequence of sample preparation process: **a** borehole drilling; **b** Pipe and micro-packer introduced in the drillhole, and detail of the end-pipe sealing system; **c** Pipe and micro-packer glued with epoxy; d) Strain gages glued to the lateral surfaces of a sample

installation of the top aluminum platen; see Sect. 3.2), air-drained, and filled with a hand syringe with the fluid used to conduct the experiments. Local strains were measured during the experiments using four 120-Ω strain gages glued with epoxy onto the four lateral surfaces of the cubic samples in three orthogonal directions (Fig. 2d): two gages in the direction of the vertical stress (σ_V), one gage in the direction of the maximum horizontal stress ($\boldsymbol{\sigma_H}$), and one gage in the direction of the minimum horizontal stress (σ_h).

3.2 Experimental setup

True-triaxial hydrofracturing testing was performed in the system illustrated in Fig. 3. A detailed description of their elements can be found in Muñoz-Ibáñez et al. (2020b). The basis of the true-triaxial system is a high-strength monobloc biaxial reaction frame (522 mm-edge, 200 mm-height and 90 mm-wall thickness) made of S355J2 + N structural steel (EN10025-2 or ASTM A572-50) (Fig. 4) where a cube-rock sample of up to 150 mm-edge may be submitted to independent loads of up to 60 MPa. Two of its internal adjacent faces are equipped with two independent, low-profile hydraulic actuators (ENERPAC CUSP150) and an aluminum (7075-T6) platen while the corresponding opposite faces count with two stiff steel spacers (S355J2 + N) plus one aluminum (7075-T6) load platen. To guarantee that the sample is geometrically centered in the frame, the added thickness of the spacers and platen is equivalent to that of the actuator (65 mm) with its load face extended to half its stroke (5 mm) and the corresponding aluminum platen. These actuators, that provide independent side-loads in two orthogonal directions (σ_H and σ_h), have a diameter of 200 mm and a maximum nominal load of 150 t (~ 1471 kN). The actuators can be governed in two ways: (1) Manually, using one or two hydraulic hand pumps connected to a manifold with distributor, check valves, etc., allowing their corresponding load balance ($\sigma_h = \sigma_H$) or imbalance ($\sigma_h \neq \sigma_H$); or (2) Automatically, using a pair of dedicated programmable high-pressure syringe-type

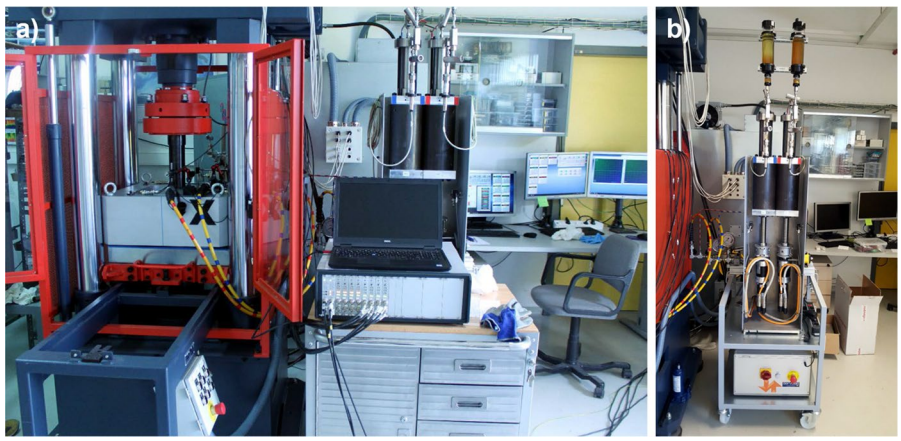

Fig. 3 Experimental setup: **a** true triaxial device placed in the servo-hydraulic press; and **b** high-pressure pumps

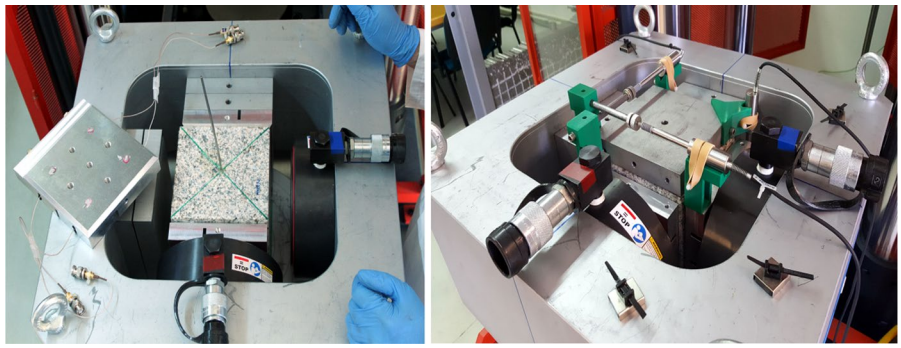

Fig. 4 Arrangement of the true-triaxial device for hydrofracturing experiments

hydraulic pumps (Fig. 3b). The actuators are single-acting, which means that, upon test completion, a small hydraulic jack is required to manually reposition them to their original (retracted) condition. The biaxial reaction frame was designed to fit into a servo-hydraulic universal press whose main actuator provides the third orthogonal loading axis (σ_V). In its present configuration, this actuator is equipped with a 1500 kN load cell that sets its current upper loading limit. When working in automatic mode, the three independent actuators (providing the magnitude for the three principal stress components: σ_1, σ_2, and σ_3) may be electronically controlled from a single computer and the dedicated programmable software PCD2K (*Servosis S.L.*). This confers a significant flexibility to the experimental system since a variety of stress paths can be designed including the possibility of axial rotation.

In order to check the limits and performance of the biaxial frame, we developed a static finite element model using the software Abaqus/Standard version 6.14 (ABAQUS 2014). The frame was modelled as a single element with the relevant material properties reported for a 200 mm-slab thickness of S355J2 + N steel. The material was assumed to behave elasto-plastically, with an elastic modulus of 210 GPa, yield strength of 285 MPa, Poisson's ratio of 0.3 and a density of 7850 kg/m^3. The frame was meshed with 4-node linear-tetrahedral elements. The loads introduced in the model were: (1) the action of the two hydraulic actuators centered in the inner faces of the frame at their maximum capacity (~46.8 MPa); and (2) the corresponding reaction of the frame associated with the presence of the opposite spacer/platens (~65.4 MPa). These loads exceed the prescribed design conditions (maximum 60 MPa at the sample face) but represent the maximum load delivered by the actuator. To this respect, the results should be understood as conservative.

The model results in terms of displacement and stress distributions are summarized in Fig. 5. We observe that the maximum stresses (~263 MPa) appear in small regions located at the inner corners of the frame. This value is ~8% below the yield strength of the steel used and far from its ultimate strength (σ_u = 450–600 MPa). However, although the stress concentration would caution us against the use of the frame in dynamic applications (if that was possible with the available actuators) at the high loads considered by the model (that are beyond the design limits of the frame), the usual working conditions considered for hydrofracturing testing should not compromise the life expectancy of the frame.

Contrary to the stress distribution, displacements are not symmetric, observing a slight difference in both horizontal directions. The larger displacements (~0.26 mm) occur at the contacts with the reaction platens (left and bottom sides in the plot; Fig. 5). This asymmetry arises from the different contact surfaces defined for frame loading: circular with 314 cm^2 (D = 200 mm) at the actuator side and squared with 225 cm^2 (150 × 150 mm^2) at the spacer edge. Based on the model results, the minimum stiffness of the biaxial frame would be ~ 6×10^9 N/m.

The top and bottom platens were manufactured with the same S355J2 + N structural steel than the frame. The top incorporates a groove to introduce the 1/8'' high-pressure stainless-steel pipe used for the injection of fluid in the sample. The four lateral platens are made of high-strength aluminum 7075-T6 alloy to reduce their weight and make them easier to handle. The aluminum platens have housing for up to 9 acoustic emission (AE) sensors each, and a circular recess in the face in contact with the sample to avoid

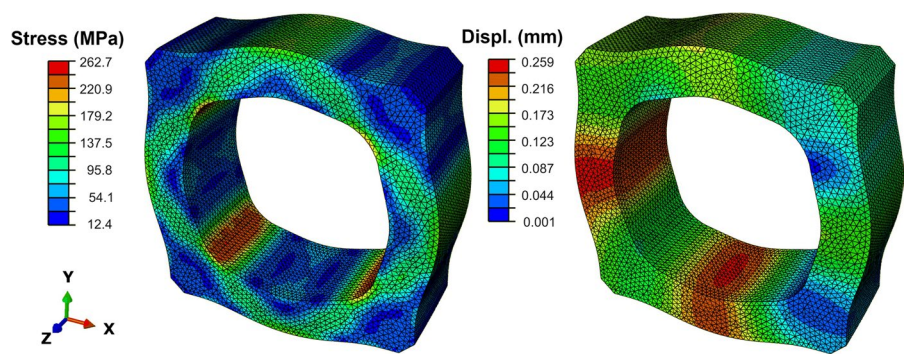

Fig. 5 Computed stress (left) and displacement (right) distributions in the true-triaxial testing biaxial frame

damages in the strain gauges eventually installed on the faces of the rock. Furthermore, the back side of these platens has grooves to bypass the electrical wires required by the different measuring devices used (e.g., AE sensors and strain gauges). The six loading platens may also be equipped with fixtures to hold three orthogonal displacement transducers (LVDT-type) useful to monitor the bulk displacements occurring in the system in the three principal stress directions. To reduce friction and avoid edge-effects, the loading platens are pre-lubricated a mixture of vaseline and stearic acid (Labuz and Bridell 1993). The edges of the platens are beveled 5 mm to avoid interaction among adjacent faces (Schwartzkopff et al. 2012), what reduces the effective loading surface on the cube to 140×140 mm^2. Consequently, the maximum load capacity of the horizontal cylinders and the vertical actuator on the samples would be ~ 75 MPa and ~ 76.5 MPa, respectively.

The injection of fluid into the rock is performed with a high-pressure syringe pump (Teledyne ISCO 100DX) operating under constant flow conditions. This pump is rated to a maximum injection pressure of 69 MPa and flow rates of up to 50 mL/min. For all the experiments reported in this work we used a mineral oil (HLP 32, ISO 6743/HM) to induce rock fracturing.

3.3 Testing procedure

In this work, hydrofacturing tests were performed under hydrostatic, normal, and strike-slip stress regime conditions. Extensional regimes (normal and, to some extent strike-slip), either in geothermics, shale gas, etc. are fairly typical in many hydraulic fracturing applications and widely documented in numerous publications. This provides a rich context where to inscribe our work. However, reverse regime scenarios have not been so well covered by experimentation and/or publications (e.g., Rahman and Abdulrazak 2013), and would require a monographic approach which is out of the limits of the present contribution.

In order to define the stress regimes and the relation between the three principal stresses for the experiments, we considered the generally accepted framework for stress distribution in the crust (e.g., Hoek 2007). The up to 35 MPa vertical stress would represent a ~ 1.5 km depth while the horizontal stresses would be consistent with an extensional context. Thus, in most of the experiments, the relation between the minimum horizontal stress and the vertical stress (σ_h/σ_V) was set to 0.4. Likewise, the relation between the minimum and maximum horizontal stresses (σ_h/σ_H) was set to 0.2 in strike-slip tests, and to 0.5 and 0.9 in normal stress regime tests. These values may be representative of a wide variety of locations. In the case of hydrostatic tests, we choose a range of confining pressures (σ_{conf}) between 0 and 35 MPa to assess the influence of the stress conditions on breakdown pressure.

The testing procedure can be split into two consecutive stages. First, the sample is confined to attain a prescribed target stress condition. Then, the hydrofracturing fluid is injected at a prescribed flow rate in two or more injection cycles. Sample confinement conforms to the desired stress path and, whenever the stress values are coincident, they are rose simultaneously. In a first stage, the magnitude of the three principal stresses increases hydrostatically up to attaining that corresponding to the minimum stress (σ_3), which in this study corresponds to the minimum horizontal stress (σ_h), or to the confining stress ($\sigma_{conf}=\sigma_h=\sigma_H=\sigma_V$) in hydrostatic tests. Then, while keeping constant the σ_3 value, load is increased simultaneously again in the other two directions. This ends when reaching the prescribed value for the intermediate stress (σ_2), which corresponds to maximum horizontal stress (σ_H) if the test is performed under a normal stress regime condition ($\sigma_V \geq \sigma_H \geq \sigma_h$), or to the vertical stress, if the test performed is strike-slip ($\sigma_H \geq \sigma_V \geq \sigma_h$). Finally, keeping constant σ_2 and σ_3, the load is increased on the third axis up to the value of the maximum stress (σ_1). The loading rate is adjusted so that the target stress is reached within 10 min since the beginning of each step. At the corresponding end, the newly attained stress situation is kept steady during a minimum of 5 min to allow the mechanical stabilization of the system.

In the fluid injection stage, the hydrofracturing fluid is delivered through the 1/8″ stainless steel pipe at a low-flow constant-rate (0.025–0.050 mL/min) to reduce the chance of fast unstable fracture propagation to the boundaries of the sample once breakdown pressure is attained. If the fracture is preserved within the physical limits of the sample, it is possible to repeat one or more injection cycles to complete the experiment by enhancing fracture propagation. In a

conventional test, the flow rate in the reinjection stage is the same as that of the first cycle although in certain situations it may be informative to decrease or increase it.

Although the displacements and strains were measured continuously in all the tests, their assessment and interpretation are out of the scope of this work.

4 Results

We have performed a total of 15 experiments across a range of confining pressures including hydrostatic, normal, and strike-slip regimes. For each regime, we have selected a subset of two representative experiments useful to analyze the evolution of the injection curves.

4.1 Hydrostatic tests

The breakdown pressures obtained from the hydrostatic tests ($P_{B,EXP}$) are reported in Table 1 and plotted in Fig. 6 as a function of confining pressure. Values of P_B estimated using the models of Abou-Sayed ($P_{B,AS}$) and Rummel ($P_{B,RU}$) are also provided for comparison. To do this, we have used the average reported value of K_{IC} for the Blanco Mera granite (1.23 MPa $m^{1/2}$; Muñoz-Ibáñez et al. 2021), and a pre-existing fracture length (a) of 2 mm based on the average grain size of this rock as reported by Arzúa and Alejano (2013). We observe that, with the exception of test #11, the difference between the experimental P_B value and the ones estimated using fracture mechanics-based models is lower than 13%.

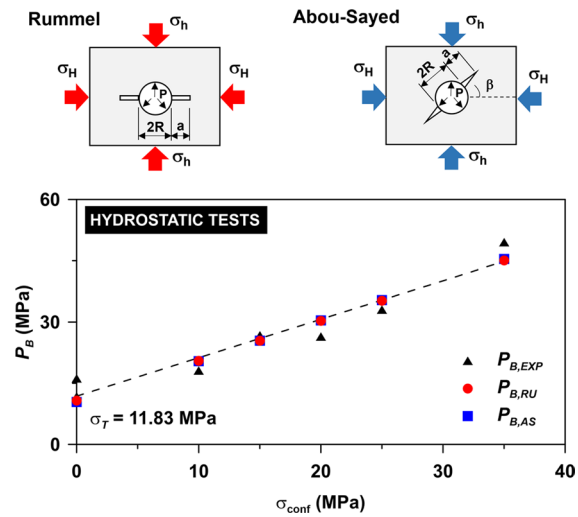

Fig. 6 Top: Schematic illustration of Rummel´s (left) and Abou-Sayed´s (right) methods. Bottom: Breakdown pressures (P_B) as a function of confining pressure (σ_{conf}) associated with the hydrostatic tests performed. Values of P_B estimated using the models of Abou-Sayed ($P_{B,AS}$) and Rummel ($P_{B,RU}$) are also plotted for comparison

Although the difference may be within an acceptable limit, it must be noted that the value of fracture toughness and the length of the pre-existing defects present some variability and that, consequently, they may have an impact on the estimated $P_{B,RU}$ and $P_{B,AS}$. On one hand, to assess the effect of mode I fracture toughness, we considered a wide range of K_{IC} values (1.1–1.4 MPa $m^{1/2}$) keeping the value of $a = 2$ mm. For $P_{B,RU}$, the maximum difference with respect to $P_{B,EXP}$ would be of 23%, while in the case of $P_{B,AS}$, the difference would increase up to 26%. On the

Table 1 Results of hydrostatic tests

Test	σ_v (MPa)	σ_H (MPa)	σ_h (MPa)	$P_{B,EXP}$ (MPa)	$P_{B,RU}$ (MPa)	%	$P_{B,AS}$ (MPa)	%
#1-S2	0	0	0	11.78	10.73	9.79	10.41	13.11
#2-S2	10	10	10	18.11	20.53	−11.80	20.41	−11.29
#3-S2	20	20	20	26.46	30.33	−12.76	30.41	−13.00
#11	0	0	0	16.17	10.73	50.65	10.41	55.27
#4	15	15	15	26.76	25.43	5.22	25.41	5.30
#7	25	25	25	33.06	35.23	−6.16	35.41	−6.65
#8	35	35	35	49.5	45.03	9.93	45.41	9.00

σ_v Vertical stress, σ_H Maximum horizontal stress, σ_h Minimum horizontal stress, $P_{B,EXP}$ Experimental breakdown pressure, $P_{B,RU}$ Computed Rummel's breakdown pressure, $P_{B,AS}$ Computed Abou-Sayed's breakdown pressure

other hand, by keeping the value of K_{IC} = 1.23 MPa $m^{1/2}$ and varying the length of the pre-existing defect (1–3 mm), the difference between the breakdown pressure estimated using both models and the experimental results would also remain below 23%.

Interestingly, as observed in Fig. 6, the values of $P_{B,AS}$ and $P_{B,RU}$ are consistent with the linear fit performed only with the experimental values. According with it, the relationship existing between $P_{B,EXP}$ and σ_{conf} may be represented as follows:

$$P_{B,EXP} = 0.94\sigma_{conf} + 11.83 \quad (12)$$

In this equation, the independent term corresponds to the breakdown pressure for unconfined conditions ($\sigma_{conf} \sim 0$) and this value can be interpreted as the tensile strength of the material, so that σ_T = 11.83 MPa.

Figure 7 shows the injection curve obtained from the hydraulic fracturing test performed at a confining stress of 10 MPa (#2-S2). In this plot, we observe that P_{prop} is greater than the confining stress what, according to what was previously explained, is the expected behavior. Furthermore, since pumping was arrested at this point (when the fracture was still not fully developed), it was possible to proceed with a second injection cycle. Based on that, the tensile strength of the rock can be assessed with Eq. (11), and this value turns out to be 10.91 MPa. It must be noted that, as shown in Fig. 7, in this experiment P_r was estimated from the pressure where the non-linear phase starts.

In contrast, the trends observed for the experiment performed at a confining stress of 20 MPa (#3-S2; Fig. 7) differ. Although the value of $P_{B,EXP}$ obtained seems reasonable, and the deviation from the theoretical models limited (error ~ 13%), the injection curve displays a steep pressure drop following breakdown pressure. In fact, the pressure falls to an intriguing value below that of confining stress. The likely explanation for that behavior is not straightforward and we conjecture a fast (complete) propagation of the fracture at the onset of P_B, and immediately followed by a sudden squirt flow and fracture closing. In this line, the tensile strength derived from Eq. (11) is more than twice the expected value for this rock (22.21 MPa) but close to that of confining pressure (20 MPa). In fact, in contrast to what happened with the experiment #2-S2, where fracturing showed the expected radially-distributed pattern of a hydrostatic compression regime (Fig. 8a), the analysis of the

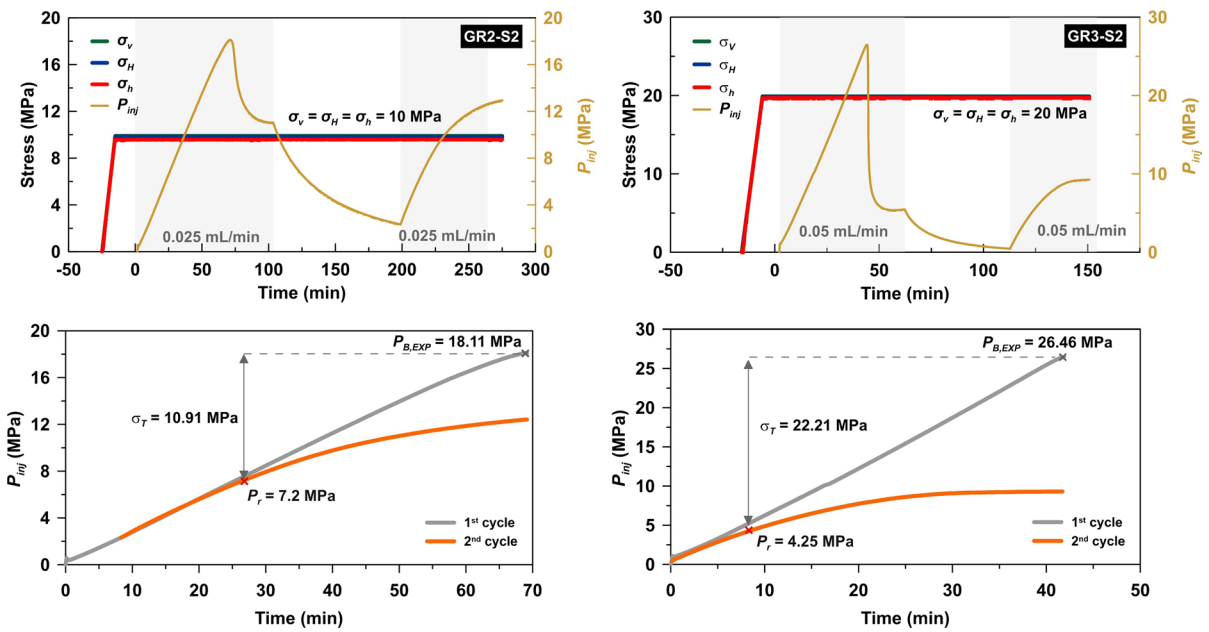

Fig. 7 Injection curve obtained from hydrostatic tests: #2-S2 (left) and #3-S2 (right)

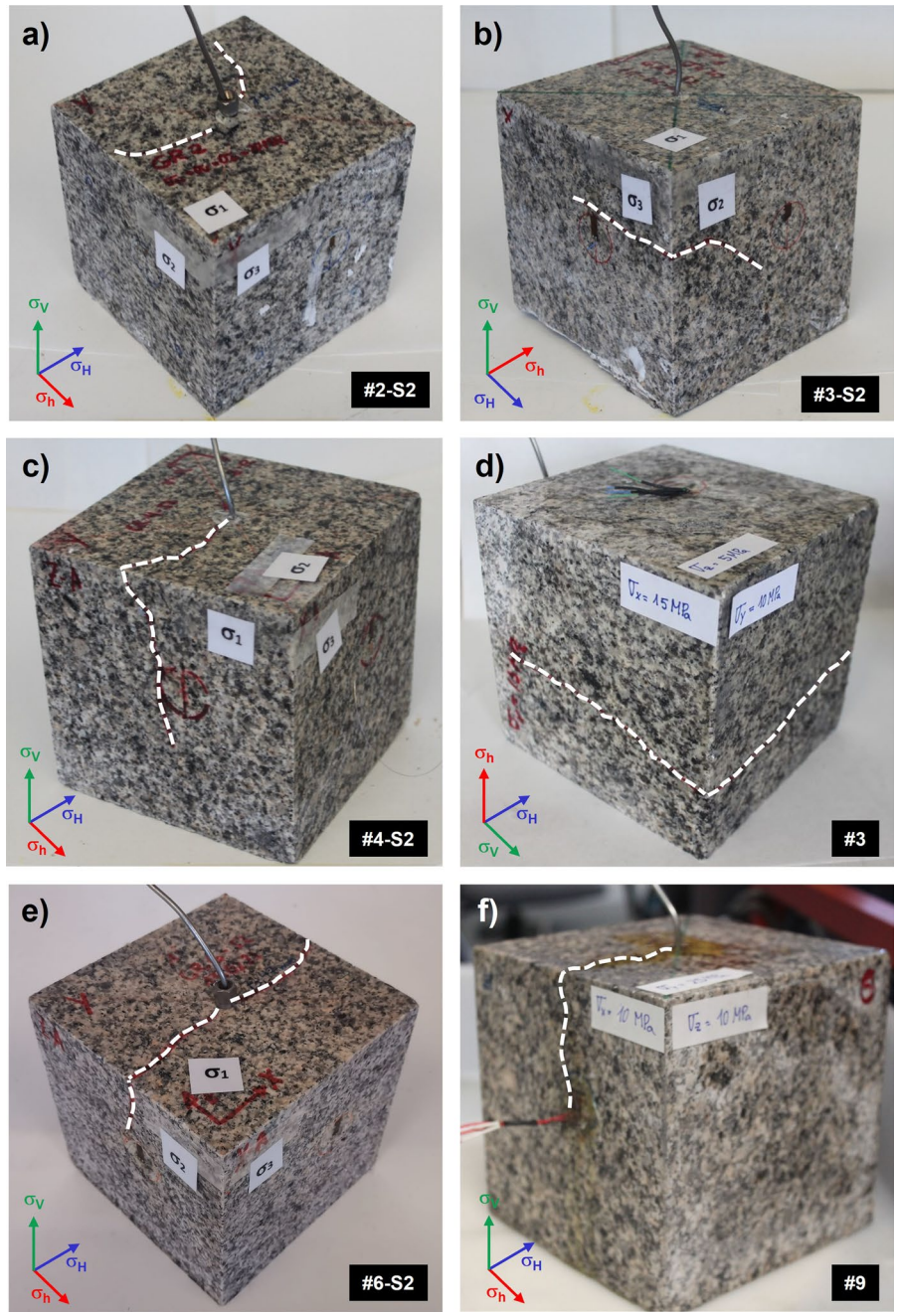

Fig. 8 Blanco Mera granite samples after failure. The white dashed lines mark the location of the hydraulic fracture with respect the applied stress field. Hydrostatic tests: #2-S2 (**a**) and #3-S2 (**b**). Strike-slip tests: #4-S2 (**c**) and #3 (**d**); Normal regime tests: #6-S2 (**e**) and #9 (**f**)

sample #3-S2 after that experiment (Fig. 8b) revealed that the hydraulic fracture was generated in an unexpected location far from the drillhole (although obviously connected). Therefore, while $P_{B,EXP}$ may still be representative of the hydrofracturing of the rock, its late behavior is likely biased by the existence in the sample of non-apparent structural weakness planes.

4.2 Strike-slip tests

Following the same approach as that described for hydrostatic tests, the breakdown pressure experimental results ($P_{B,EXP}$) as well as those corresponding to the theoretical models ($P_{B,AS}$ and $P_{B,RU}$) for the strike-slip regime ($\sigma_H \geq \sigma_V \geq \sigma_h$) experiments are

Table 2 Results of strike-slip tests

Test	σ_v (MPa)	σ_H (MPa)	σ_h (MPa)	$P_{B,EXP}$ (MPa)	$P_{B,RU}$ (MPa)	%	$P_{B,AS}$ (MPa)	%
#4-S2	5	10	2	11.78	11.73	0.42	11.47	2.74
#5-S2	10	20	4	14	12.73	9.99	12.52	11.85
#3	10	15	5	16.37	14.43	13.45	14.23	15.05

σ_v Vertical stress, σ_H Maximum horizontal stress, σ_h Minimum horizontal stress, $P_{B,EXP}$ Experimental breakdown pressure, $P_{B,RU}$ Rummel's breakdown pressure, $P_{B,AS}$ Abou-Sayed's breakdown pressure

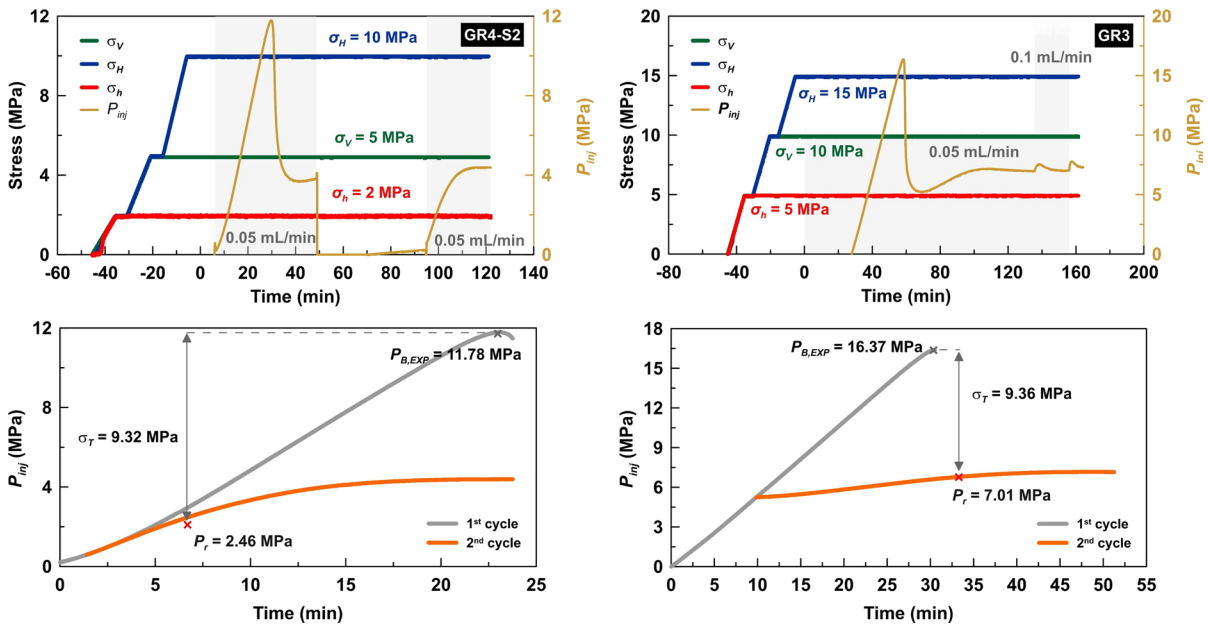

Fig. 9 Injection curve obtained from strike-slip tests: #4-S2 (left) and #3 (right)

reported in Table 2. Like in the previous case, the error observed for this series of tests is lower than 15%.

Figure 9 shows the injection curves for tests #4-S2 and #3, respectively. In both cases and as expected, P_{prop} is greater than σ_h. However, P_c could not be estimated for any of the experiments: while in test #4-S2, due to a data acquisition issue, the injection pressure was not recorded upon pump arrest, in test #3 the two injection cycles were performed consecutively (i.e., without stopping the injection) and at a different pumping rate. In any case, the computed values for tensile strength seem to be in line with those derived from hydrostatic tests (9.32 and 9.36 MPa for tests #4-S2 and #3, respectively).

Regarding the orientation of the fractures, we observe that the pattern is the same in the three experiments executed, with fractures developing in a plane perpendicular to σ_h (Fig. 8c, d) and crosscutting the injection drillhole. Due to the heterogeneity of the Blanco Mera granite, fractures did not form simultaneously at both sides of the sample, as also reported by Zhuang et al. (2020a) for Pocheon granite.

4.3 Normal regime tests

As shown in Table 3, for the tests performed under a normal stress regime condition ($\sigma_V \geq \sigma_H \geq \sigma_h$), and, with the exception of test #6-S2, the error observed between the experimental and estimated values of breakdown pressure was considerably higher when compared with hydrostatic or strike-slip regime experiments.

Table 3 Results of normal regime tests

Test	σ_v (MPa)	σ_H (MPa)	σ_h (MPa)	$P_{B,EXP}$ (MPa)	$P_{B,RU}$ (MPa)	%	$P_{B,AS}$ (MPa)	%
#6-S2	12.5	10	5	14.85	15.03	−1.21	14.82	0.19
#7-S2	25	20	10	12.17	19.33	−37.04	19.23	−36.71
#8-S2	22.5	10	9	15.15	19.43	−22.04	19.30	−21.49
#9-S2	45	20	18	33.39	28.13	18.70	28.18	18.50
#9	25	10	10	12.58	20.53	−38.73	20.41	−38.38

σ_v Vertical stress, σ_H Maximum horizontal stress, σ_h Minimum horizontal stress, $P_{B,EXP}$ Breakdown pressure, $P_{B,RU}$ Rummel's breakdown pressure, $P_{B,AS}$ Abou-Sayed's breakdown pressure

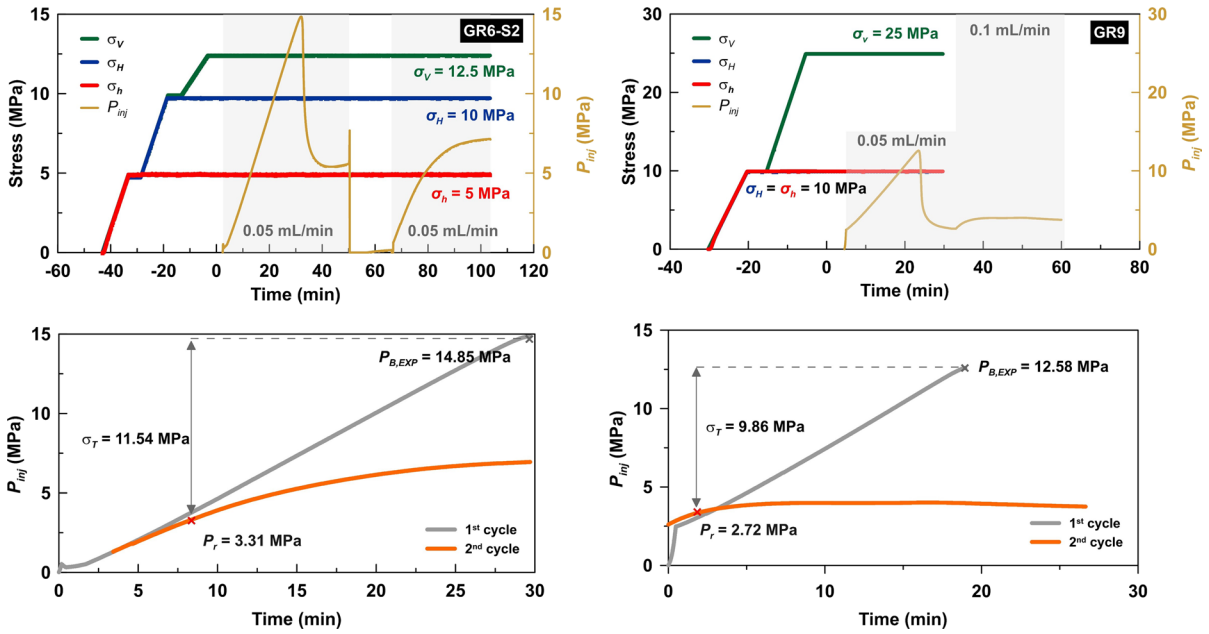

Fig. 10 Injection curve obtained from normal stress regime test #6-S2 (left) and #9 (right)

The injection curve recorded for test #6-S2 (Fig. 10) provides with consistent results in terms of the fracture propagation pressure ($P_{prop}=5.45$ MPa $>\sigma_h=5$ MPa) and tensile strength ($\sigma_T=11.54$ MPa). Furthermore, the orientation of the fracture was perpendicular to the σ_h (Fig. 8e). However, missed data about injection pressure during inter-cycle pump arrest makes not possible the assessment of the fracture closure pressure P_C.

Test #9 (Fig. 10) displayed an anomalous behavior. Although the value of P_{prop} (2.61 MPa) is significantly smaller than the minimum stress applied (10 MPa), the computed value for its tensile strength (9.86 MPa) is in good agreement with the ones obtained in the previous tests, and the orientation of the hydraulic fracture was consistent with the distribution of stresses (i.e., perpendicular to σ_h; Fig. 8f).

5 Discussion

5.1 Breakdown and re-opening pressures

The values of breakdown pressure (P_B) obtained in this work for Blanco Mera granite are comparable to those reported in previous published studies for similar rock types. Li et al. (2022) performed

a series of true triaxial hydraulic fracturing tests on cubic (length = 100 mm) granite samples under normal stress conditions (σ_v = 25 MPa; σ_H = 3–9 MPa; σ_h = 3 MPa). The values of P_B obtained by these authors varied between ~ 6–14 MPa, in agreement with those shown in Table 3 for similar loads (P_B ~ 12–15 MPa). For the same sample size but under strike-slip conditions (σ_H = 6 MPa; σ_v = 4 MPa; σ_h = 3 MPa), Zhuang et al. (2020a) report higher breakdown pressures (P_B ~ 13–19 MPa) for Pocheon granite than those obtained here for similar loading conditions (P_B = 11.78 MPa, test #4-S2). Higher values of breakdown pressure (P_B = 9–25 MPa) are reported by Chen et al. (2015) for the same stress regime but using a slightly larger sample (length = 170 mm) of Kurokami-jima granite. In fact, factors such as sample size, stress state, or injection rate, may produce variations in breakdown pressure, and they should be taken into account when comparing experimental results (Zhuang and Zang 2021).

The seminal models of Hubbert and Willis (1957) and Haimson and Fairhurst 1969) assume a stress distribution around the borehole based on the Kirsch (1898) equations. Kirsch's solution allows to calculate the radial, circumferential, and shear stresses around a cylindrical cavity, and may be used to anticipate fracture initiation pressures (Fig. 11a). The formulation is applicable to an infinite plane containing a circular hole that is subjected to far-field compressive stresses. It also considers that the material surrounding the hole is isotropic, homogeneous, and linearly elastic. In hydrofracturing, this may be a more or less precise approach if the borehole can be represented by a 2D-cross section enclosed within a pair of packers. However, if the domain of interest is close to the bottom of the borehole (like in the experiments presented in this work) and the fluid is injected into a test interval where this is an effective boundary of the system, the pressure exerted by the fluid would not only be applied to the lateral surfaces of the borehole but also downwards (Fig. 11b). In this configuration (known as single packer; Yihdego 2017), Kirsch's equations are no longer applicable, and the blind implementation of these conventional approaches may lead to inaccurate predictions.

On the other hand, the fracture mechanics approaches (i.e., Rummel's and Abou-Sayed's models) used in this work for estimating P_B have provided acceptable results, especially in the case of hydrostatic and strike-slip regime tests. Mohamadi et al. (2021) and Gao et al. (2020) have also reported improved prediction of stress magnitudes based on fracture mechanics models. Their results highlight the importance of considering in the interpretation of hydraulic fracturing tests the existence of pre-existing defects, and therefore the fracture toughness of the material. However, although these defects may have a great influence in stress determination (Mohamadi et al. 2021; Gao et al. 2020), it is not less challenging to estimate their associated length (Zhuang and Zang 2021). In this work, this was approached based on a low-sophistication

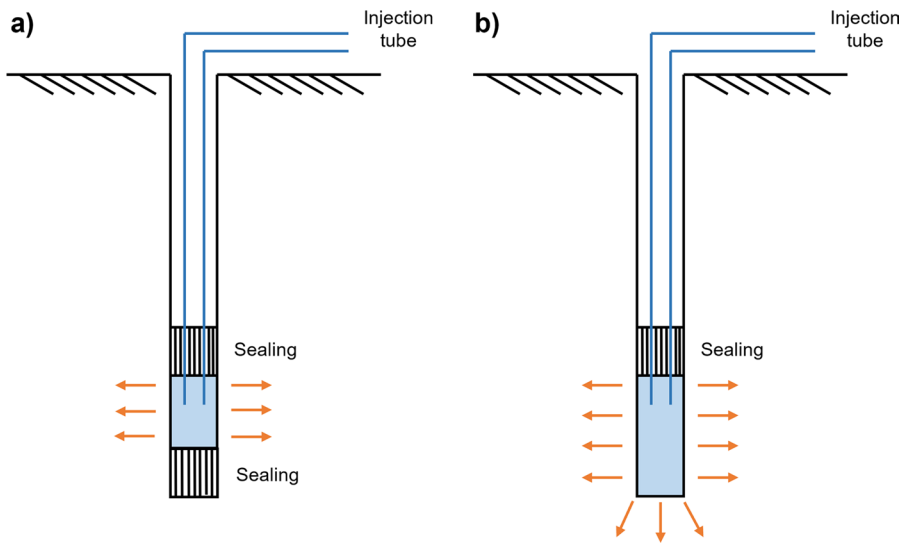

Fig. 11 Schematic showing fluid injection: **a** double packer; **b** single packer. Adapted from Hamm et al. (2007) and Jiang et al. (2009)

visual inspection of the grain size and grain contacts of Blanco Mera granite. Accepting that this can be improved with advanced instrumental techniques, it is noteworthy that the results obtained have been satisfactory. On the other hand, the models developed by Rummel (1987) and Abou-Sayed et al. (1978) to assess P_B, contrary to the traditional equations, do not require information about the tensile strength of the material. This may be advantageous because the determination of σ_T may not be straightforward, as we discuss below.

To explain fracture initiation in brittle materials, finite fracture mechanics (FFM) integrates two failure criteria: 1) the stress criterion, which assumes that failure occurs when the stress applied overcomes the tensile strength of the material ($\sigma = \sigma_T$); and 2) the energy criterion, which considers that failure takes places when the strain energy becomes equal to the critical energy release rate, i.e. the energy needed to create new crack surfaces ($G = G_C$). Under pure mode I and plane strain conditions, the critical energy release rate (G_{IC}) for a crack can be related to the fracture toughness (K_{IC}) through the relationship proposed by Irwin (1957):

$$G_{IC} = {K_{IC}}^2 \left(\frac{1 - \nu^2}{E} \right) \tag{13}$$

where E is the Young's modulus of the material. Considering the previous criteria, Sapora et al. (2022) applied the FFM approach to a pressurized circular hole and derived an expression useful to compute the failure (breakdown) pressure under unconfined conditions:

$$P_{B,FFM} = \sqrt{\frac{2,10}{R}} K_{IC} \tag{14}$$

These authors found a good agreement between this theoretical prediction and the experimental data previously obtained in hydrofracturing tests of cylindrical hollow samples of the Lac du Bonet granite and Indiana limestone. However, the estimated mode I fracture toughness ($K_{IC} = 0.35$–0.37 MPa $m^{1/2}$) that was obtained based on fitting Eq. (14) to the experimental results, was considerably lower (2–3 times) than that obtained by the direct measurement of this property. Similarly, if we apply Eq. (14) to the two tests performed without confining pressure (#1-S2 and #11) as part of this study, the mode I fracture toughness for Blanco Mera granite would range between 0.45–0.61 MPa $m^{1/2}$, which is lower than the values previously reported for the same material (Muñoz-Ibañez et al. 2021). This suggests that the FFM model presented above may overestimate the breakdown pressure by 200% and, therefore, these models should be applied with caution.

In the tests presented in this work, the reopening pressure (P_r) is not clearly manifest as a second maximum following breakdown pressure in the injection curve. For this reason, the value of P_r was determined from the plots of P_{inj} *vs.* time, at the point in which the curve becomes non-linear. As suggested by Bröker and Ma (2022), this would be related to a decrease in stiffness of the hydraulic system when the fracture reopens in a second injection cycle. For Rotondo granite, these authors report reopening pressures between ~ 11–19 MPa. Although these values are significantly larger than those obtained in this work (P_r ~ 3–7 MPa), they could be consistent if we take into account that the difference between P_B and P_r (i.e., the tensile strength) is in the range 5.4–11.6 MPa (see Sect. 5.3). Similarly, the higher reopening pressures (P_r ~ 5–10 MPa) obtained by Enever and Chopra (1986) also result in similar values of σ_T (8–14 MPa). As mentioned above, the variations in P_r observed could be attributed to the different experimental conditions in which the tests were performed.

5.2 Instantaneous shut-in (ISIP) and fracture closure pressures (PC)

Considering the six hydrofracturing tests described in this work, the only experiment in which the injection curve (P_{inj}) was properly recorded after P_B was test #2-S2 ($\sigma_{conf} = 10$ MPa). Therefore, we used the results from this test to assess the instantaneous shut-in pressure (ISIP) and fracture closure pressure (P_c). In this case, after injection stops, a sharp drop in pressure is not observed and therefore ISIP cannot be clearly identified. According to Doe and Vietor (2014), ISIP can be more easily recorded in impervious materials, which typically display an insignificant pressure decline after ISIP. This behavior contends with our observations for Blanco Mera granite, for which injection pressure drops continuously after shut-in.

In an attempt to assess ISIP and following the inflection point method (Bröker and Ma 2022), it was

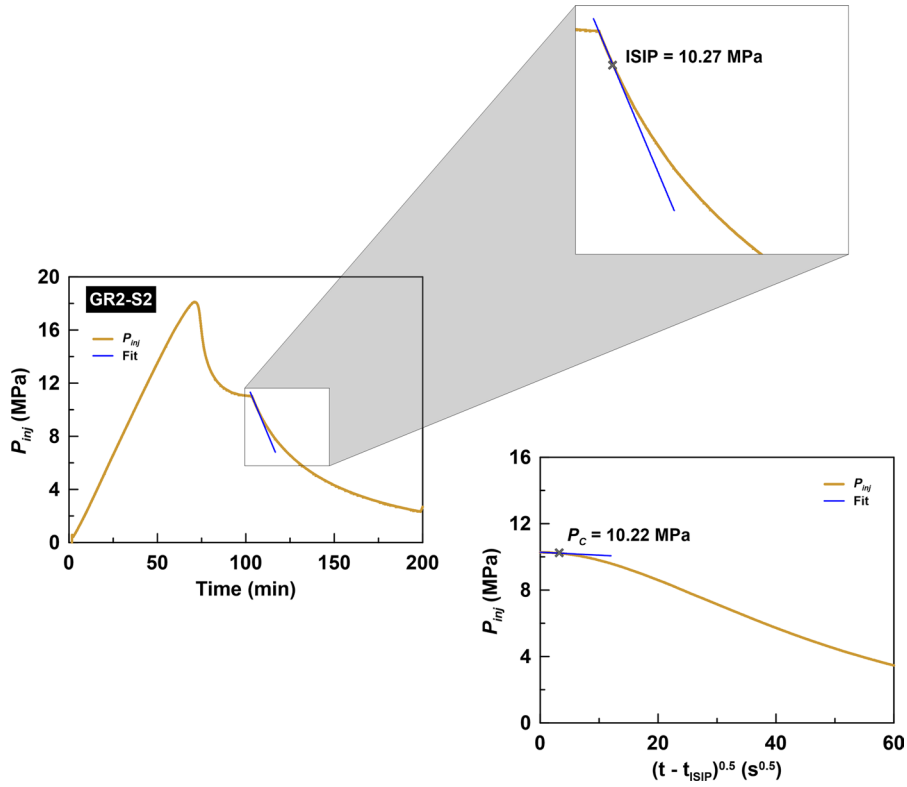

Fig. 12 Determination of instantaneous shut-in pressure (ISIP) and closure pressure (P_C) in test #2-S2

estimated at the point where the injection curve deviates from a tangent line directly after pump shut-in (Fig. 12). Then, the fracture closure pressure (P_C) was evaluated as the pressure at which there is a change in leak-off regime, that is, the value at which the plot pressure vs $t_{ISIP}^{1/2}$ (where t_{ISIP} is the time after shut-in) departs from a linear trend (Bröker and Ma 2022). As a result, the values of ISIP and P_C determined for this particular test were 10.27 and 10.22 MPa, respectively, which are approximately equal the confining stress (σ_{conf} = 10 MPa). Although the values seem satisfactory, suggesting that the stress concentration generated by the drillhole might not be significant (as described in Sect. 2.2), the results are based on a limited amount of experiments, and should be confirmed by further testing.

5.3 Tensile strength

The tensile strength of the material tested was approached using three different methods: 1) based on the pressure difference between $P_{B,EXP}$ and P_r (with the exception of tests #3-S2, the values of tensile strength obtained from the tests described above are in good agreement and provide an average value of $\sigma_T = 10.20 \pm 0.99$ MPa); 2) from the value of $P_{B,EXP}$ in tests performed at ambient pressure (σ_T = 11.78–16.17 MPa); and 3) from the independent term in the linear fit of hydrostatic tests (σ_T = 11.83 MPa). The values of σ_T obtained from the three methods are quite consistent among them and, although slightly greater, they are also in line with the magnitude of tensile strength determined previously in Brazilian tests reported for this rock (σ_T = 8.5–10.5 MPa; Muñoz-Ibáñez et al. (2020a); Pérez-Rey et al. (2022)). A similar observation was also reported by Molenda et al. (2013) for the tensile strength of six different rock types obtained from Brazilian disc tests and minifrac tests.

Although the minor differences observed can be attributed to rock heterogeneities, it must be noted also that both breakdown pressure and re-opening pressure are flow-rate dependent (Cheng and Zhang 2020), and therefore the values of tensile strength obtained may also be influenced by this factor. Furthermore, and as reported by Cuisiat and Haimson (1992), the size of the drillhole may cause a scale effect in hydraulic fracturing, with larger drillholes

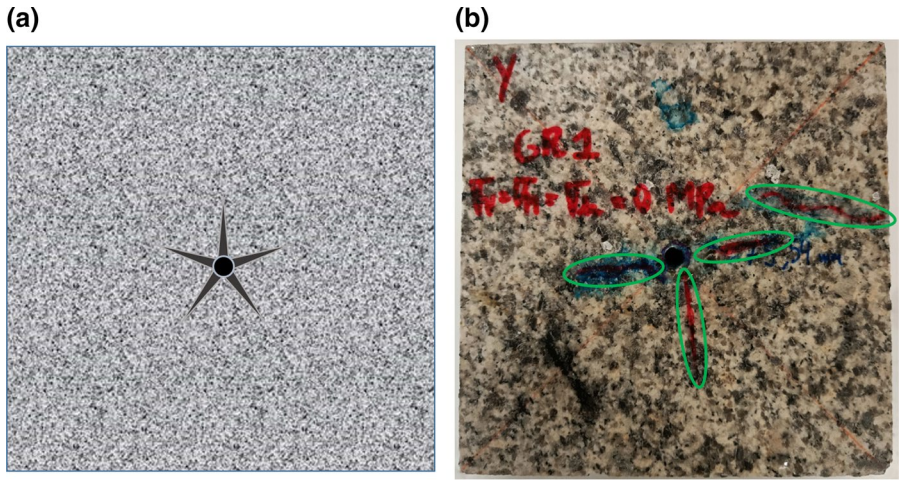

Fig. 13 Radial fracture generation under hydrostatic conditions: **a** Theoretical fracture pattern; and **b** Blanco Mera granite sample after testing in the absence of confining pressure ($\sigma_V = \sigma_H = \sigma_h = 0$)

providing smaller values of P_B. Consequently, the tensile strength of the rock may also vary with the size of the borehole. All these factors should be considered when assessing tensile strength measurements from hydrofracturing tests, and special care should be taken in the cases when the hydraulic fracture does not clearly reopen in a second reinjection cycle (Gao et al. 2020), like in test #3.

5.4 Hydraulic fracture orientations

In hydro-fracturing tests, tensile fractures develop as a consequence of the progressive increase of pressure induced by the injection of fracturing in the sample and, provided that a number of constrains are met (e.g., sample homogeneity), their orientation should be consistent with the imposed stress field. The orientation of hydraulic fracture planes for strike-slip and normal stress regime tests were approximately perpendicular to the minimum principal stress (σ_h) and crosscutting the injection drillhole located in the geometrical center of the sample cubes. The variability in the location of the fracture planes among samples may be a result of the natural heterogeneity of the rock (i.e., local microstructure effect) around the injection volume. Furthermore, they may be also influenced by rock anisotropy, which in granite can be caused by non-apparent weakness planes or cleavages (rift), as well as more apparent foliations (e.g., mafic clusters; Zhuang and Zang 2021). These features, together with the existence of natural fractures of different scales, can affect the fracture pattern, which can vary depending on the orientation of the discontinuities with respect to the loading configuration (Chang et al. 2022; Zhang et al. 2022a).

On the other hand, under hydrostatic conditions, hydraulic fractures should have an equal probability of generation in all directions and, as a result, various of them may appear distributed radially around the drillhole (e.g., Fig. 13). However, even in this case, the onset of fracturing and their propagation may be significantly affected by rock properties, including mineralogy, grain size, texture, and heterogeneity (Zhuang and Zang 2021). Although in our hydrostatic tests the fractures were mainly produced close to the region drillhole, we also observed some fractures manifesting far from the injection point. In these cases, the likely presence of pre-existing defects in the rock may have acted as stress concentrators and constrained the location (and propagation) of fractures (Zhuang et al. 2020b). This may be further complicated by other interferences such as fracture coalescence or interlocking what, in turn, will affect the assessment of breakdown pressure values, since fluid flow would not only be limited to a single fracture.

6 Conclusions

We have conducted true-triaxial hydrofracturing experiments under different stress regime conditions (hydrostatic, strike-slip and normal) using Blanco Mera granite specimens. From this study, the following conclusions are drawn:

(1) The fracture mechanics-based models proposed by Abou-Sayed and Rummel can provide reasonably satisfactory results for the interpretation of hydrofracturing tests, especially for hydrostatic and strike-slip tests.
(2) Taking into account that the experimental conditions (e.g., sample size, stress state, injection rate, drillhole radius, etc.) may have an influence on breakdown (P_B) and reopening (P_r) pressures, the acceptability of the tests was verified by assessing the coherence of derived parameters, such as tensile strength (σ_T), independently of the stress regime applied.
(3) The value of mode I fracture toughness (K_{IC}), which is a function of the size of pre-existing defects, seems to have a strong influence on the interpretation of hydrofracturing results, especially when using finite fracture mechanics (FFM) models. In this regard, the application of FFM can lead to significant overestimations of P_B or underestimations of K_{IC}.
(4) Despite the above-mentioned aspects, there are still intrinsic uncertainties associated with the role of non-apparent mechanical heterogeneities (e.g., rifts), mineral and/or textural heterogeneities (e.g., exfoliation of certain minerals, concentration of mafic minerals) or micro- and meso-defects in the matrix, which may condition the experimental results. Although the imposed stress field has a strong influence on the location and orientation of hydraulic fractures, the presence of these features can alter the expected fracturing behavior.

To deal with the previous aspects, it would be desirable to improve the level of knowledge with techniques that provide information about the inner characteristics of the samples before (ultrasonic waves) and during (ultrasonic waves, acoustic emission) the execution of the tests. Finally, it would be interesting to model the behaviour observed in the tests and complementary measurements (strains, acoustic activity, etc.) with the aim of establishing constitutive models for these materials, susceptible to be upscaled.

Acknowledgements This work was funded by REPSOL S.A. and the support of the Spanish Ministry of Science and Innovation (PID2021-126419NB-I00). A. Muñoz-Ibáñez also acknowledges the Margarita Salas grant from the Spanish Ministry of Universities, funded by the European Union – Next Generation EU. Funding for open access charge: Universidade da Coruña/CISUG.

Author contribution AMI: investigation, formal analysis, visualization and writing—original draft; MHP: investigation, formal analysis and visualization; JDM: conceptualization, methodology, funding acquisition, project administration, supervision and writing—review & editing; LAM: methodology, funding acquisition, supervision and writing—review & editing; JCV: conceptualization, methodology and funding acquisition; JAI: conceptualization, methodology and funding acquisition.

Funding Open Access funding provided thanks to the CRUE-CSIC agreement with Springer Nature. This work was funded by REPSOL S.A. and the support of the Spanish Ministry of Science and Innovation (PID2021-126419NB-I00). A. Muñoz-Ibáñez also acknowledges the Margarita Salas grant from the Spanish Ministry of Universities, funded by the European Union – Next Generation EU.

Data availability All the data generated and analyzed during this study are available from the corresponding author on reasonable request.

Declarations

Competing interests On behalf of all authors, the corresponding author states that there is no conflict of interest.

Ethics approval and consent to participate Not applicable.

Consent for publication Not applicable.

References

ABAQUS (2014) ABAQUS Version 6.14 / Analysis user's guide. Dassault Systemes Simulia Corporation, Providence, Rhode Island

Abou-Sayed AS, Brechtel CE, Clifton RJ (1978) In situ stress determination by hydrofracturing: a fracture mechanics approach. J Geophys Res 83:2851. https://doi.org/10.1029/JB083iB06p02851

Alejano LR, Estévez-Ventosa X, González-Fernández MA et al (2021) A method to correct indirect strain measurements in laboratory uniaxial and triaxial compressive strength tests. Rock Mech Rock Eng 54:2643–2670. https://doi.org/10.1007/s00603-021-02392-4

Arzúa J, Alejano LR (2013) Dilation in granite during servo-controlled triaxial strength tests. Int J Rock Mech Min Sci 61:43–56. https://doi.org/10.1016/j.ijrmms.2013.02.007

Bérard T, Chugunov N, Desroches J, Prioul R (2019) Feasibility and design of hydraulic fracturing stress tests using a quantitative risk assessment and control approach. Petrophysics 60:113–135. https://doi.org/10.30632/PJV60N1-2019a9

Bi Z, Wang L, Yang H et al (2021) Experimental study on the initiation and propagation of multi-cluster hydraulic fractures within one stage in horizontal wells. Energies (basel). https://doi.org/10.3390/en14175357

Biot MA (1941) General theory of three-dimensional consolidation. J Appl Phys 12:155–164

Bröker K, Ma X (2022) Estimating the least principal stress in a granitic rock mass: systematic mini-frac tests and elaborated pressure transient analysis. Rock Mech Rock Eng. https://doi.org/10.1007/s00603-021-02743-1

Cao W, Yildirim B, Durucan S et al (2021) Fracture behaviour and seismic response of naturally fractured coal subjected to true triaxial stresses and hydraulic fracturing. Fuel. https://doi.org/10.1016/j.fuel.2020.119618

Chang Z, Hou B, Ding J (2022) Competitive propagation simulation of multi-clustered fracturing in a cracked shale oil reservoir. Geomech Geophys Geo-Energy Geo-Resour 8:1–19. https://doi.org/10.1007/s40948-022-00399-x

Chen Y, Nagaya Y, Ishida T (2015) Observations of fractures induced by hydraulic fracturing in anisotropic granite. Rock Mech Rock Eng 48:1455–1461. https://doi.org/10.1007/s00603-015-0727-9

Cheng Y, Zhang Y (2020) Experimental study of fracture propagation: the application in energy mining

Cuisiat FD, Haimson BC (1992) Scale effects in rock mass stress measurements. Int J Rock Mech Min Sci Geomech Abstr 29:99–117. https://doi.org/10.1016/0148-9062(92)92121-R

Doe T, Vietor T (2014) Review of in situ stress measurements and their context. Mont Terri Project, TR2012-06

Enever JR, Chopra PN (1986) Experience with hydraulic fracture stress measurements in granite. In: Proceedings of the international symposium on rock stress and rock stress measurements, stockholm. pp. 411–420

Feng Y, Jones JF, Gray KE (2015) Pump-in and flow-back tests for determination of fracture parameters and in-situ stresses. In: AADE National technical conference and exhibition 11

Frash LP, Gutierrez M, Hampton J (2014) True-triaxial apparatus for simulation of hydraulically fractured multi-borehole hot dry rock reservoirs. Int J Rock Mech Min Sci 70:496–506. https://doi.org/10.1016/j.ijrmms.2014.05.017

Gao G, Wang C, Zhou H, Wang P (2020) Modified fracture mechanics approach for hydraulic fracturing stress measurements. Geofluids. https://doi.org/10.1155/2020/8860163

Gehne S, Forbes Inskip ND, Benson PM et al (2020) Fluid-driven tensile fracture and fracture toughness in nash point shale at elevated pressure. J Geophys Res Solid Earth 125:1–11. https://doi.org/10.1029/2019JB018971

Guo H, Aziz NI, Schmidt LC (1993) Rock fracture toughness determination by the Brazilian test. Eng Geol 33:177–181

Haimson BC (1980) Near-surface and deep hydrofracturing stress measurements in the Waterloo quartzite. Int J Rock Mech Min Sci Geomech Abstr 17:81–88. https://doi.org/10.1016/0148-9062(80)90260-0

Haimson B, Fairhurst C (1969) Hydraulic fracturing in porous-permeable materials. J Petrol Technol 21:811–817

Hamm SY, Kim MS, Cheong JY et al (2007) Relationship between hydraulic conductivity and fracture properties estimated from packer tests and borehole data in a fractured granite. Eng Geol 92:73–87. https://doi.org/10.1016/j.enggeo.2007.03.010

Hoek E (2007) In situ and induced stresses. In: Practical rock engineering

Huang B, Liu J (2017) Experimental investigation of the effect of bedding planes on hydraulic fracturing under true triaxial stress. Rock Mech Rock Eng 50:2627–2643. https://doi.org/10.1007/s00603-017-1261-8

Hubbert MK, Willis DG (1957) Mechanics of hydraulic fracturing. Pet Trans AIME 210:153–163

Irwin GR (1957) Analysis of stresses and strains near the end of a crack transversing a plate. J Appl Mech 24:361–364

Jiang XW, Wan L, Wang XS et al (2009) Estimation of rock mass deformation modulus using variations in transmissivity and RQD with depth. Int J Rock Mech Min Sci 46:1370–1377. https://doi.org/10.1016/j.ijrmms.2009.05.004

Kirsch G (1898) Die theorie der elastizitat und die bedurfnisse der festigkeitslehre. Veit Deit Ing 42(28):797–807

Lee MY, Haimson BC (1989) Statistical evaluation of hydraulic fracturing stress measurement parameters. Int J Rock Mech Min Geomech Abstr 26:447–456. https://doi.org/10.1016/0148-9062(89)91420-4

Li N, Xie H, Gao Z, Li C (2022) Study on the hydraulic fracturing failure behaviour of granite and its comparison with gas fracturing. Sustainability 14:14593. https://doi.org/10.3390/su142114593

Liu Y, Li M, Yin G et al (2018) Permeability evolution of anthracite coal considering true triaxial stress conditions and structural anisotropy. J Nat Gas Sci Eng 52:492–506. https://doi.org/10.1016/j.jngse.2018.02.014

Lu YL, Elsworth D, Wang LG (2013) Microcrack-based coupled damage and flow modeling of fracturing evolution in permeable brittle rocks. Comput Geotech 49:226–244. https://doi.org/10.1016/j.compgeo.2012.11.009

Lu Y, He M, Wu B, Meng X (2020) Experimental and theoretical analysis of hydraulic fracturing and gas fracturing of rock under true triaxial compressions. Eng Fract Mech 234:107100. https://doi.org/10.1016/j.engfracmech.2020.107100

Malik M, Jones C, Edward B (2016) How can microfracturing improve reservoir management? In: Paper presented at the SPWLA 57th Annual Logging Symposium, Reykjavik, Iceland

Mohamadi A, Behnia M, Alneasan M (2021) Comparison of the classical and fracture mechanics approaches to determine in situ stress/hydrofracturing method. Bull Eng Geol Environ. https://doi.org/10.1007/s10064-021-02184-8

Molenda M, Stöckhert F, Brenne S, Alber M (2013) Comparison of hydraulic and conventional tensile strength tests. In: ISRM International conference for effective and sustainable hydraulic fracturing 2013, International society for rock mechanics, pp. 981–992

Morawietz S, Heidbach O, Reiter K et al (2020) An open-access stress magnitude database for Germany and adjacent regions. Geotherm Energy. https://doi.org/10.1186/s40517-020-00178-5

Muñoz-Ibáñez A, Delgado-Martín J, Costas M et al (2020a) Pure mode I fracture toughness determination in rocks using a pseudo-compact tension (pCT) test approach. Rock Mech Rock Eng 53:3267–3285. https://doi.org/10.1007/s00603-020-02102-6

Muñoz-Ibáñez A, Delgado-Martín J, Juncosa-Rivera R et al (2020b) Development of a true triaxial device for hydraulic fracturing experiments. In: Rock mechanics for natural resources and infrastructure development- Proceedings of the 14th international congress on rock mechanics and rock engineering, ISRM 2019. CRC Press/Balkema, pp 1195–1202

Muñoz-Ibáñez A, Delgado-Martín J, Juncosa-Rivera R (2021) Size effect and other effects on mode I fracture toughness using two testing methods. Int J Rock Mech Mining Sci 143:104785. https://doi.org/10.1016/j.ijrmms.2021.104785

Ødegaard H, Nilsen B (2021) Rock stress measurements for unlined pressure tunnels: a true triaxial laboratory experiment to investigate the ability of a simplified hydraulic jacking test to assess fracture normal stress. Rock Mech Rock Eng 54:2995–3015. https://doi.org/10.1007/s00603-021-02452-9

Patel SM, Sondergeld CH, Rai CS (2018) Hydraulic fracture permeability estimation using stimulation pressure data. Int J Rock Mech Min Sci 101:50–53. https://doi.org/10.1016/j.ijrmms.2017.11.013

Pérez-Rey I, Muñoz-Ibáñez A, González-Fernández MA et al (2022) Size effects on the tensile strength and fracture toughness of granitic rock in different tests. J Rock Mech Geotech Eng. https://doi.org/10.1016/j.jrmge.2022.11.005

Rahman MM, Abdulrazak MKA (2013) Enhancing oil production from tight formations under a reverse faulting stress regime by multistage fracturing. Energy Sour Part A Recovery Util Environ Eff 35:2242–2249. https://doi.org/10.1080/15567036.2012.658138

Rummel F (1987) Fracture mechanics approach to hydraulic fracturing stress measurements. In: Atkinson BK (ed) Fracture mechanics. Academic Press Inc., London, pp 217–240

Sapora A, Efremidis G, Cornetti P (2022) Non-local criteria for the borehole problem: gradient elasticity versus finite fracture mechanics. Meccanica 57:871–883. https://doi.org/10.1007/s11012-021-01376-6

Schwartzkopff AK, Priest S, Melkoumian N, Egudo JA (2012) Design and fabrication of a low cost true triaxial cell for testing multiple size specimens. In: Kwasniewski M, Li X, Takahashi M (eds) True triaxial testing of rocks. CRC Press, pp. 83–95. https://doi.org/10.1201/b12705

Song I, Suh M, Won KS, Haimson B (2001) A laboratory study of hydraulic fracturing breakdown pressure in table-rock sandstone. Geosci J 5:263–271. https://doi.org/10.1007/BF02910309

Yihdego Y (2017) hydraulic in situ testing for mining and engineering design: packer test procedure, preparation, analysis and interpretation. Geotech Geol Eng 35:29–44. https://doi.org/10.1007/s10706-016-0112-9

Zeng F, Guo J, Ma S, Chen Z (2018) 3D observations of the hydraulic fracturing process for a model non-cemented horizontal well under true triaxial conditions using an X-ray CT imaging technique. J Nat Gas Sci Eng 52:128–140. https://doi.org/10.1016/j.jngse.2018.01.033

Zhang B, Ji B, Liu W (2018) The study on mechanics of hydraulic fracture propagation direction in shale and numerical simulation. Geomech Geophys Geo-Energy Geo-Resour 4:119–127. https://doi.org/10.1007/s40948-017-0077-z

Zhang Y, Yin S, Zhang J (2021a) In situ stress prediction in subsurface rocks: an overview and a new method. Geofluids. https://doi.org/10.1155/2021/6639793

Zhang P, Liang X, Xian C et al (2022a) Geomechanics simulation of stress regime change in hydraulic fracturing: a case study. Geomech Geophys Geo-Energy Geo-Resour 8:1–18. https://doi.org/10.1007/s40948-022-00391-5

Zhang Y, Ge H, Zhao K et al (2022b) Simulation of pressure response resulted from non-uniform fracture network communication and its application to interwell-fracturing interference in shale oil reservoirs. Geomech Geophys Geo-Energy Geo-Resour. https://doi.org/10.1007/s40948-022-00422-1

Zhang JJ (2019) Geomechanics applications in hydraulic fracturing. In: Applied petroleum geomechanics. Elsevier, pp 441–481. https://reader.elsevier.com/reader/sd/pii/B9780128148143120015?token=E92BE05CE9B17759A4A29489EEB97BD999714B90A8534F50C17FB877C3C75A1FC2C5FC841AA521D2DE1B4E964EBD9EF&originRegion=euwest-1&originCreation=20230309085932

Zhu G, Dong S (2022) Discrete element simulation model of pulsating hydraulic fracturing considering fatigue damage. Geomech Geophys Geo-Energy Geo-Resour. https://doi.org/10.1007/s40948-022-00424-z

Zhuang L, Zang A (2021) Laboratory hydraulic fracturing experiments on crystalline rock for geothermal purposes. Earth Sci Rev 216:103580. https://doi.org/10.1016/j.earscirev.2021.103580

Zhuang L, Jung SG, Diaz M et al (2020a) Laboratory true triaxial hydraulic fracturing of granite under six fluid injection schemes and grain-scale fracture observations. Rock Mech Rock Eng 53:4329–4344. https://doi.org/10.1007/s00603-020-02170-8

Zhuang L, Kim KY, Diaz M, Yeom S (2020b) Evaluation of water saturation effect on mechanical properties and hydraulic fracturing behavior of granite. Int J Rock Mech Min Sci 130:104321. https://doi.org/10.1016/j.ijrmms.2020.104321